ORIGINAL PAPER

Kidney damage in extracorporeal shock wave lithotripsy: a numerical approach for different shock profiles

Kerstin Weinberg · Michael Ortiz

Abstract In shock-wave lithotripsy—a medical procedure to fragment kidney stones—the patient is subjected to hypersonic waves focused at the kidney stone. Although this procedure is widely applied, the physics behind this medical treatment, in particular the question of how the injuries to the surrounding kidney tissue arise, is still under investigation. To contribute to the solution of this problem, two- and three-dimensional numerical simulations of a human kidney under shock-wave loading are presented. For this purpose a constitutive model of the bio-mechanical system kidney is introduced, which is able to map large visco-elastic deformations and, in particular, material damage. The specific phenomena of cavitation induced oscillating bubbles is modeled here as an evolution of spherical pores within the soft kidney tissue. By means of large scale finite element simulations, we study the shock-wave propagation into the kidney tissue, adapt unknown material parameters and analyze the resulting stress states. The simulations predict localized damage in the human kidney in the same regions as observed in animal experiments. Furthermore, the numerical results suggest that in first instance the pressure *amplitude* of the shock wave impulse (and not so much its exact time-pressure profile) is responsible for damaging the kidney tissue.

Keywords Kidney · Soft tissue · Injury · Damage · Large deformation · Constitutive model · Cavitation · Shock wave · Finite element analysis

K. Weinberg (✉)
Institute of Mechanics (MS2), Technical University of Berlin,
Einsteinufer 5, 10587 Berlin, Germany
e-mail: kerstin.weinberg@tu-berlin.de

M. Ortiz
Division of Engineering and Applied Science,
California Institute of Technology, Pasadena, CA 91125, USA

1 Introduction

Extracorporeal shock-wave lithotripsy (ESWL) is the most common treatment for kidney stone disease. The idea of this non-invasive procedure is to generate high intensity pressure waves (shock waves) outside the patient and to focus them on the stone to fragment it, see Fig. 1. The therapy was developed over twenty years ago and is well established meanwhile. For kidney stones of 10–20 mm size it has proven to be fast, effective, and relatively free from the trauma and expense associated with surgery.

In an ESWL treatment the urologist controls three parameters: the number of shock waves administered, the repetition rate, and the voltage (or energy) of the shock wave generator. The latter is directly associated to the amplitude of the pressure wave. Typically, from one to three thousand shock waves are fired onto the stone at a rate of around one per second. The treatment of stone comminution is monitored by fluoroscopy or ultrasound and terminated when the residual fragments are small enough to be voided in the urine.

A very important factor in the treatment is the lithotripter device, because it determines the profile of the ESWL impulse. Different types of lithotripters are classified by the type of shock wave source they utilize (for details see, e.g., Thiel et al. 2000; Wess 2004).

The most common lithotripters are electro-hydraulic devices, e.g., the Dornier HM3, which generate shock waves by underwater spark discharge. The waves are focused by a brass ellipsoidal reflector to an area of approximately 10–15 mm in diameter and with peak pressures in the range of 30–50 MPa. A typical pressure measurement at the focus of a HM3 lithotripter is shown in Fig. 2.[1] A narrow positive

---

[1] Data courtesy of Michael R. Bailey, Center for Industrial and Medical Ultrasound, Applied Physics Lab, University of Washington, Seattle.
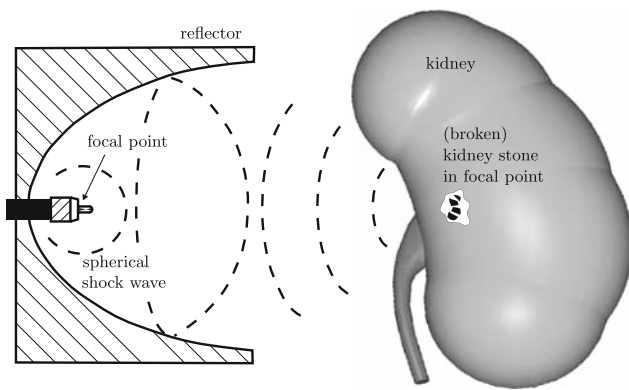
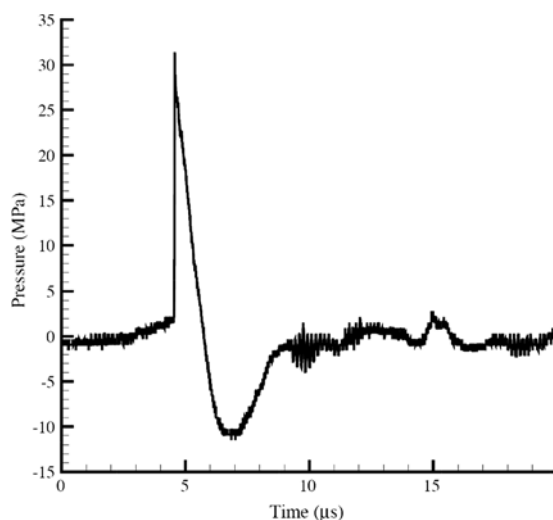**Fig. 1** Principle of shock wave induced destruction of kidney stones (ESWL)

pressure spike with short rise time and rapid fall (<1 μs) is followed by a significant negative pressure, the so called "tension tail".

An analytical expression of such an ESWL impulse was given in Howle et al. (1998)

$$p(t) = \begin{cases} 2p_{\max} \exp^{-t/\tau_1} \cos\left(\frac{t}{\tau_2} + \frac{\pi}{3}\right) & \text{if } 0 < t < \frac{7\pi}{6}\tau_2, \\ 0 & \text{otherwise.} \end{cases}$$

$$(1)$$

The time variables τ_1 and τ_2 determines the profile of the ESWL impulse, τ_1 characterizes the pressure decay and τ_2 the duration. We will specify these values later.

In this contribution we provide results of two- and three-dimensional finite element analyses (FEAs) of a shock wave treatment of a kidney, and we study the effect of different profiles of ESWL impulses on the soft tissue.

Following this introduction we shortly explain the mechanisms of stone breakage and tissue damage. In Sect. 3 we introduce a detailed finite element model and calibrate the elastic properties of the tissue material to map a realistic wave transmission. Section 4 is devoted to a discussion of the experimental data available to quantify the inelastic material properties of kidney tissue. In Sect. 5 we present the underlying mechanical theory, in particular, the constitutive relation to describe damage in the soft tissue. The concluding Sect. 6 summarizes the results and show that, despite of a high uncertainty in the material data, the FEAs predict the locations of damaged regions in good agreement to clinical and experimental studies.

2 Basic physical principles

The widespread use of lithotripsy and potential side effects, has originated numerous research efforts aimed at understanding the physics of ESWL.

The exact mechanisms of **stone breakage** are still a topic of debate, but two mechanisms have been substantiated by empirical observation:

Spallation is a material failure caused by tensile stress. Tension is induced as the compressive part of the pressure wave is reflected by the distal stone–tissue interface as a tensile wave. The reflected wave combines with the tensile tail of the incident wave to produce a plane of maximum tensile stress that can cleave the stone.

Erosion is caused by the action of cavitating bubbles near the stone. The tensile wave component typically generates bubbles (or clouds of bubbles) that oscillate in

(a) experimentally measured ESWL impulse
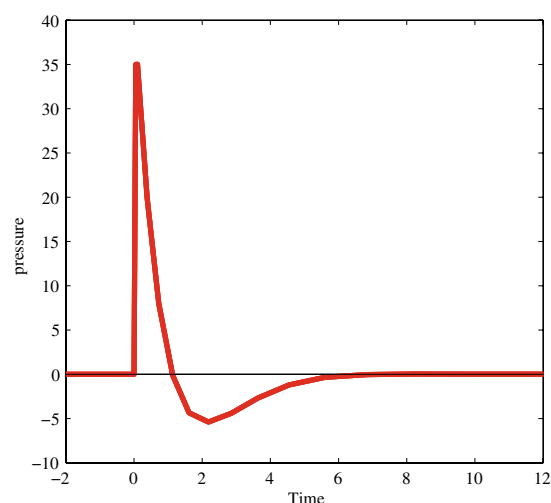
(b) mathematical model of the ESWL impulse

Fig. 2 Experimentally measured ESWL impulse at the focal point of a HM3 lithotripter and impulse after Eq. (1)

Fig. 3 Illustration of **a** symmetric and **b** asymmetric oscillations of bubbles with jetting created during asymmetric collapse and **c** typical solution of the Rayleigh–Plesset equations for spherical bubbles subjected to a pressure impulse, cf. Brennen (1995)
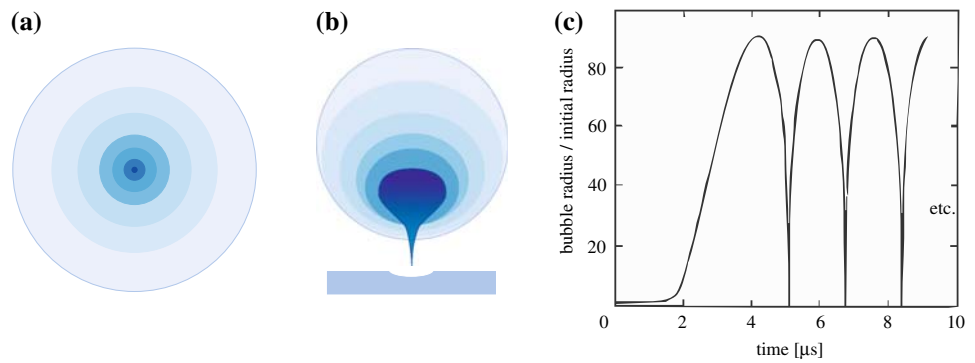
size and collapse violently after the passage of the wave. Bubble cavitation in fluids can be described by means of the Rayleigh–Plesset equation: see Tanguay and Colonius (2003) and Fig. 3 for a typical solution. Cavitation is an important comminution mechanism and responsible for the pitted surfaces of the disintegrated stone, cf. Coleman and Saunders (1993) and Bailey et al. (2003b).

Although effective in breaking kidney stones, ESWL can also cause significant short- and long-term damage to the kidneys as reported in Brown et al. (2000), Chaussy et al. (2002), Evan et al. (1998) and Willis et al. (1999) and many others. Experimental investigations on rats and pigs followed with the aim to understand the reasons for tissue damage caused by shock waves (Blomgren et al. 1997; Connors et al. 2000; Deng et al. 1993). In particular, the pig kidney is similar in structure and function to a human kidney, thus making it a useful model for understanding the human kidney. The extent of kidney injuries depends on many factors, e.g., the size of the kidney, the blood pressure, the age of the patient, etc. However, it is not yet completely clear what the exact injuring mechanisms in the kidney tissue are and, in particular, how these structural and functional values change when the parameters of an ESWL treatment are varied. Typical lesions in the kidney are bruising, renal and perirenal hemorrhage and kidney enlargement, see Fig. 4. Generally, two mechanical effects seem to be essential:

Tissue shearing: The compressive wave of the ESWL impulse needs a high peak pressure to induce spallation in the stone. However, the focused wave front induces shearing and stretching along its way through the kidney tissue. The induced **shear stress** may be responsible for kidney injuries in the pre-focal area (Sturtevant and Lokhandwalla 1998; Coleman et al. 1995).

Tension: The compressive front is followed by a tension tail and, therefore, bubbles cavitate and may expand up to several micrometers in size. During bubble expansion the surrounding vessels and capillaries dilate and may rupture. This mechanism causes irreversible changes of
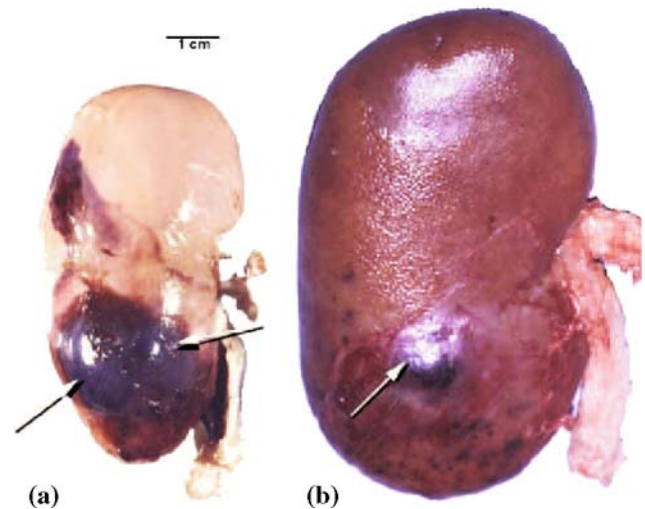

Fig. 4 Typical kidney injuries after an ESWL treatment observed on **a** a small juvenile and **b** a larger adult pig kidney, both subjected to the same dosage of treatment, cf. Blomgren et al. (1997). The figure illustrates how difficult it is to generally quantify the amount of tissue injury and how it correlates with the degree of functional change

the kidney tissue due to **hydrostatic tension** (Bailey et al. 2003a; Zhong et al. 2001; Coleman et al. 1995).

Furthermore, experimental evidence suggests that tissue damage is solely caused by subjecting the kidney tissue to shock waves; the presence or absence of a kidney stone does *not* affect the side effects (Wilson et al. 1992). Thence the kidney is modeled without a stone in all presented computations.

3 Calibration of the finite element model of a human kidney

The (two) kidneys are part of the urinary system, located just above the waist in the human abdomen. A typical kidney in an adult is 10–12 cm long, 5–7 cm wide and 3-cm thick and has a mass of 135–150 g. The concave medical border of each kidney faces the vertebral column; near the center is a vertical fissure through which ureter and blood vessels leave the kidney. A frontal section through the kidney reveals two distinct

(a) surface data   **(b)** surface data   **(c)** geometry of the finite element mesh
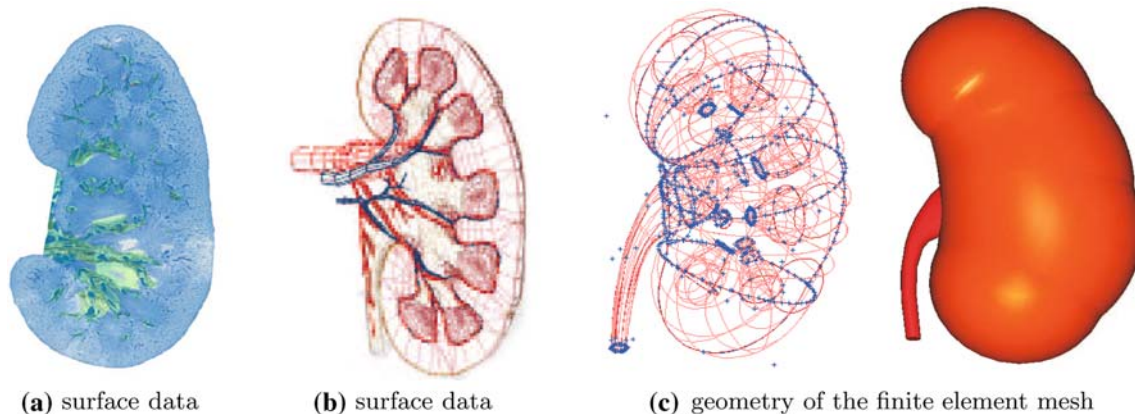
Fig. 5 Frontal section of a left kidney (Photograph courtesy of Dr. A. Evans, Department of Anatomy, Indiana University School of Medicine, IA, USA.), geometrical model of one half of a human kidney and simplified geometrical model obtained from this data

regions: a superficial, smooth-textured reddish area called renal cortex (cortex = rind or bark) and a deep, reddish-brown region called the renal medulla (medulla = inner portion). Within the medulla tissue 6–10 cone shaped renal pyramids constitute the functional portion of the kidney. On the microscopic level, the functional units located here are about 1 million structures called nephrons that engage in the three basic processes: filtering blood, returning useful substances to blood and removing substances by producing urine. The urine then drains into a single large cavity, the renal pelvis, and finally out into the urinary bladder.

To study ESWL by FEAs we have initiated an effort aimed at the development of anatomically correct models of the kidney. To this end, we purchased geometrical data from a company[2] that specializes in the visualization of complex structures, see Fig. 5a. With the help of these surface data a finite element mesh including the gross anatomical details was built. It should be noted that the geometrical data, as purchased, do not fulfill appropriate requirements for a finite element mesh (i.e., non-overlapping, non-distorted elements with positive volume) and the three-dimensional finite element model generated here required significant manual manipulation. Furthermore, a simplified two-dimensional model including the main anatomical details was built, see Figs. 6 and 7 for the results.

To avoid mismatching effects from the boundaries, the kidney models are completely embedded in surrounding tissue. Altogether five regions of tissue are distinguished, representing renal cortex, pyramids, medulla tissue, ureter with renal pelvis and the surrounding body. For each of them a different material behavior can be assigned. Note that these different region are defined in the three-dimensional model as well, although they can hardly be distinguished on the pictures.

A shock wave is a type of propagating disturbance typically associated with a high stress intensity and traveling at speed higher than sound speed. However, the energy of a shock wave may be dissipated relatively quickly with distance, degenerating the shock wave into a conventional sound wave. The acoustic impedance Z of a material is given by the ratio of sound pressure p to the absolute value of particle velocity v or, equivalently, as the product of material density ρ_0 and longitudinal wave speed c_L.

$$Z = \frac{p}{|v|} = \rho_0 c_L. \tag{2}$$

Interfaces of materials with different acoustic impedance influence a wave that is traveling through it. The upper sketch in Fig. 8a illustrates a wave hitting the interface orthogonally. With indices e, r, t for entering, reflected and transmitted wave, it holds $p_e + p_r = p_t$. The normal velocity components decompose accordingly, and we define the reflection coefficient $r \in (-1, 1)$ by

$$r = \frac{p_r}{p_e} = \frac{Z_2 - Z_1}{Z_1 + Z_2}. \tag{3}$$

Cases with $r < 0$ are called *soft* reflection (or soft transmission), whereas $r > 0$ describes *hard* reflection, which is additionally characterized by *phase inversion*. The lower figure of Fig. 8a illustrates the reflection in an ideal fluid. In a real medium, and in particular in solids, the inclined interface causes not only reflection but also transverse waves to arise. Consequently, we observe a decay of magnitude and, after several reflections, a scattering of the traveling wave.

During ESWL the reflection at tissue inhomogeneities as well as the interaction with cavitating bubbles influences the traveling pressure wave. In experiments a significant decay of the wave's amplitude with the propagated distance was observed (Filipczynski et al. 1994). Figure 8b shows the amplitude of the shock impulse after penetration of kidney

---

2 Viewpoint Corporation, New York; http://www.viewpoint.com.
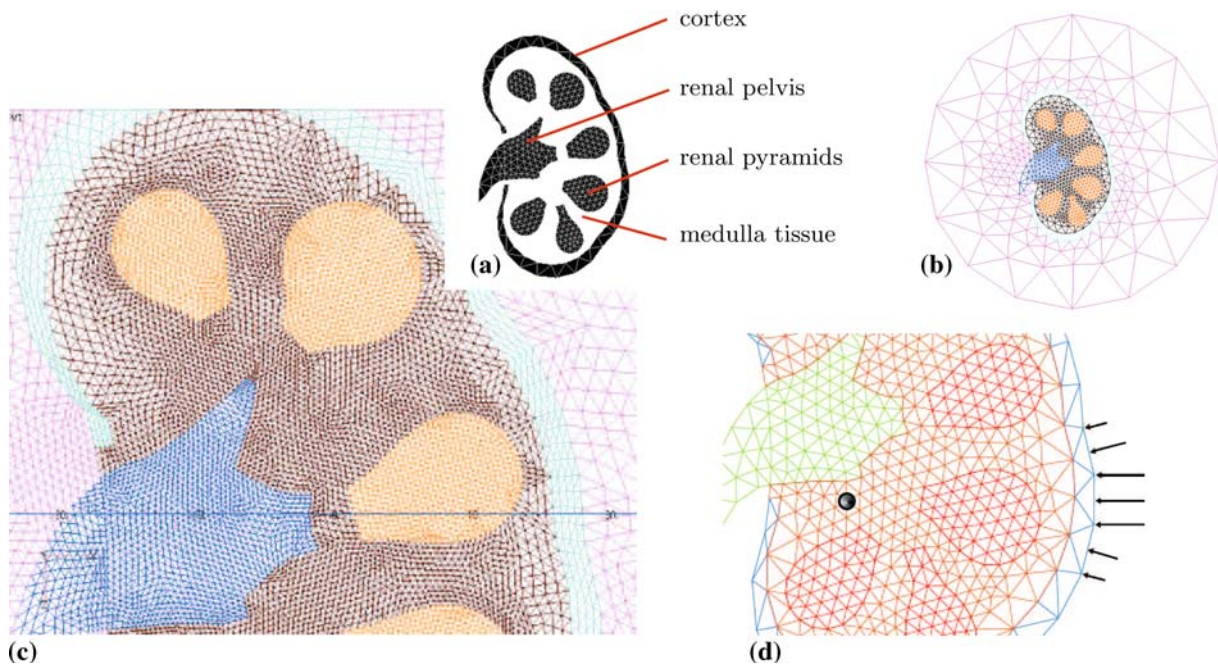
Fig. 6 Two-dimensional model of the kidney: **a** regions of different materials, **b, c** finite element mesh and **d** loaded boundary, the focus ("stone") is marked with "•"

Fig. 7 Three-dimensional finite element model of a kidney: **a** mesh and applied load at the kidney surface represented as nodal velocity v_y (mm/μs), **b** full model of the kidney embedded in an acoustic material, where the side length of the displayed box is 20 cm, **c** meridional section of the kidney, which is about 12×7 cm in size. The coordinate system in **a** is moved to the left because its origin is located in the meridional section, 1 cm above the focal point
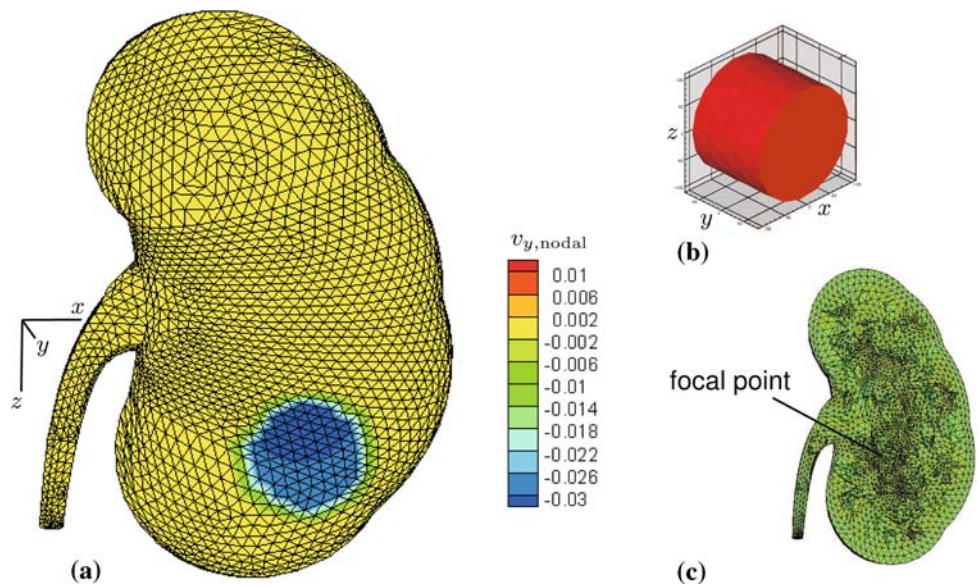
samples of 5, 10, 25 and 40 mm thickness, which decays to 2/3 of its initial value (after 40 mm).

To calibrate our finite element model we studied at first the propagation of a pressure impulse in a homogeneous elastic model meshed with triangular plain strain elements (quadratic shape functions). The uniaxial sample with a Young modulus of $E = 1$ MPa is free in the axial but constrained in the lateral direction. The pressure impulse is given by Eq. (1) with $\tau_1 = 1.1$ μs, $\tau_2 = 1.96$ μs and $p_{max} = 100$ MPa. To prescribe the loading impulse as a nodal velocity we use the linear relation between pressure and particle velocity (2)

$$v = \frac{p}{\varrho_0 \, c_L}. \tag{4}$$

With measured data of $c_L = 1{,}540$ m/s and $\rho_0 = 1{,}050$ kg/m³ (Farshad et al. 1999; Maass and Kuehnapfel 1999, cf. Sect. 5) and $c_L = \sqrt{\kappa/\rho_0}$ we directly determine the bulk modulus of the kidney to be $\kappa = 2{,}500$ MPa. (Note that this

Fig. 8 Wave reflection and transmission ($\sin \alpha / c_1 = \sin \beta / c_2$) and peak positive pressure measured in Filipczynski et al. (1994) after penetration of calf kidney samples of different thickness up to 40 mm

(a) wave reflection

(b) ESWL penetration
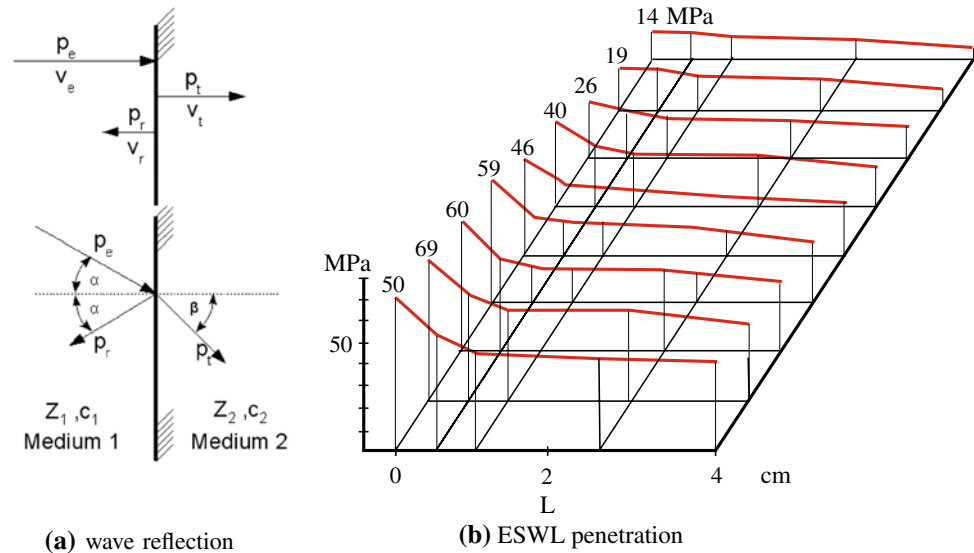
value is slightly above the compressibility of water $\kappa_{H_2O} = 2{,}250$ MPa.)

For coarse meshes, we observe after short distances of wave travel a rapid decay in amplitude and high oscillations following the initial impulse. Refining the mesh reduces the decay but still shows high frequency oscillations. Therefore, we introduced an artificial (bulk) viscosity which generates a viscosity pressure as a linear function of the volumetric strain rate $\dot{\vartheta}$,

$$p_{\text{damp}} = \alpha \rho c_L l_e \dot{\vartheta}. \tag{5}$$

Here α is a damping coefficient and l_e is an element characteristic length. The artificial viscosity is thought to damp oscillations in the highest element frequency. (Note that we do *not* apply forms of artificial viscosity which are designed to smear a shock front across several elements.)

Figure 9b, c show the pressure impulse for a (carefully calibrated) damping coefficient of $\alpha = 0.06$ after 10 and 40 mm propagation, corresponding to position 1 and 3 of Fig. 9a. The high frequency oscillations are damped, but so is the pressure's amplitudes, cf. Plagemann (2006).

Figure 10 illustrates transitions at orthogonal material interfaces with different compressibility. Here we emulate both soft and hard reflection with arbitrary but likely values for the reflection coefficient (3). To this end, we vary the Young modulus of region 3, see Fig. 9a, while all other data remain constant.

Soft reflection is realized with $r = -\frac{1}{2}$ and $E_3 = \frac{1}{9}E$; for hard reflection $r = \frac{1}{2}$ it follows that $E_3 = 9E$.
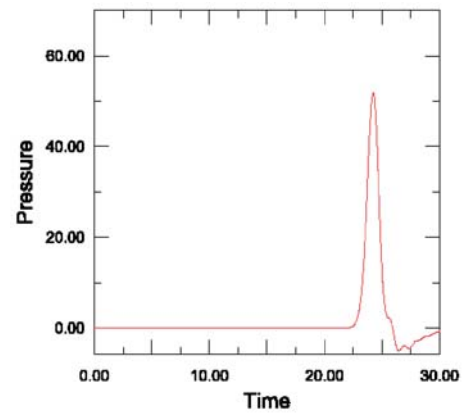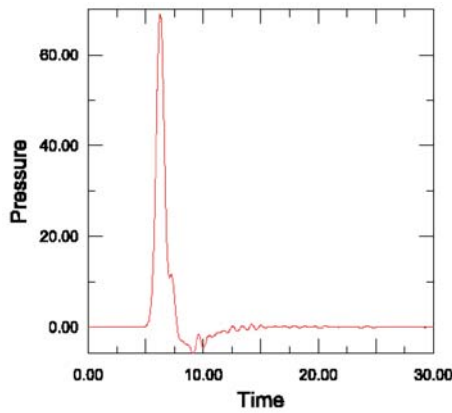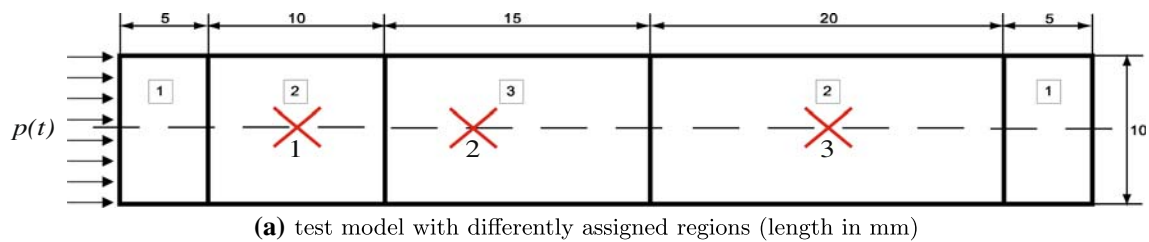
Figure 10a, c show the initial ($t = 6\,\mu s$) and reflected ($t = 12.5\,\mu s$) pressure at the marked position 1. With reflection the amplitude decays and we observe a rarefaction due to soft reflection at $t = 12.5\,\mu s$ in Figure 10a, whereas in Figure 10c we observe a compression peak due to hard

reflection. In the following the pressure magnitudes are superposed due to further reflections and interference at the material interfaces. The situation is displayed here in Fig. 10b, d, at the marked position 2 of Fig. 9a. In particular Fig. 10d shows a superposition of the first peak of Fig. 10c, travelling from left to right, superposed with the reflected second peak, travelling from right to left.

Finally, we employ the test model of Fig. 9a to vary the material parameter for the different regions of the kidney to realistically map its different elastic properties. The volumes of the materials in the test model correspond to the volume fractions of cortex (1), renal medulla (2) and pyramidal (3) tissue a ESWL impulse will pass. Assuming sound speed as a lower limit for the wave propagation speed, a time of at most $l_{\text{model}}/c_L = 35.5\,\mu s$ is needed to pass the model. Knowing that the cortex is stiffer than the average kidney, cf. Farshad et al. (1999), whereas the pyramids are likely to be softer, and summarizing different variations we set: $E_1 = 1.2$ MPa, $E_2 = 1.0$ MPa, $E_3 = 0.55$ MPa. With these elastic parameters, the time required for the impulse to traverse the tissue corresponds to a propagation with sound speed c_L.

4 Material properties of kidney tissue

Whereas the elasticity in a dynamically loaded material can be estimated from the easy to measure wave speed, cf. Maass and Kuehnapfel (1999), the inelastic properties are very difficult to quantify. Experimental investigations on kidney tissue can be found in Farshad et al. (1999), Miller (2000), Melvin et al. (1973) and Nasseri et al. (2002). The intentions of the reported experiments are different, but all available experiments have in common that they focus on the elastic and viscoelastic properties for "the" kidney, i.e., the whole organ

(a) test model with differently assigned regions (length in mm)

(b) impulse after 10 mm propagation

(c) impulse after 40 mm propagation

Fig. 9 Wave propagation after an ESWL impulse with $p_{\max} = 100$ MPa: **a** uniaxial test model where the numbers refer to regions with assigned elastic modulus E_1, E_2 and E_3, **b, c** pressure impulse (MPa) versus time (μs) after propagation into homogeneous elastic tissue $E_1 = E_2 = E_3$ computed with a mesh of quadratic elements (size ≈ 0.5 mm) and with an artificial viscosity of $\alpha = 0.06$

(a) soft: $r = -1/2$ at 2

(b) soft: $r = -1/2$ at 3

(c) hard: $r = 1/2$ at 2

(d) hard: $r = 1/2$ at 3
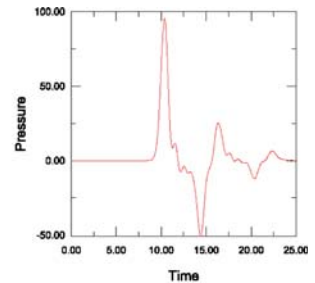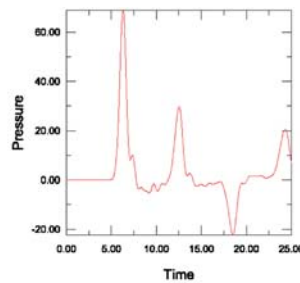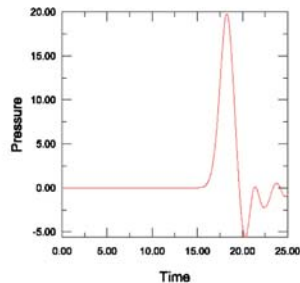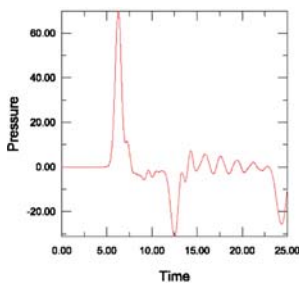
**Fig. 10** Wave propagation after an ESWL impulse with $p_{\max} = 100$ MPa: pressure impulse (MPa) versus time (μs) at position 1 and 2 in Fig. 9a after reflection and transmission

is considered to be made of an isotropic and homogenized material. The first assumption—isotropy—is justified by the irregular and non-uniformly textured tissue. The assumption of a homogenized material, however, is not helpful for our investigation, because we need to distinguish between different regions of the kidney with a different sensitivity to stress and straining.

Farshad et al. (1999) performed shear tests by punching a cylinder into a slice of 8–10 mm thickness and 40 mm diameter taken from the renal cortex of pigs. The tests were conducted on the undisturbed outer surface of the kidney (with the membrane-like hull being removed) and on a sliced section of the cortex. The corresponding rupture stress is 35 and 25 kPa, see Fig. 11. The latter is of particular interest for us because the measurement is obtained from a "pre-damaged" cut portion of the material, which is likely to correspond better to our situation where bubble cavitation induces (micro)damage in the tissue. Note that in this specimen at a certain point the stress level is not increased by further straining, i.e., the specimen shows somewhat like a "plastic" region. Moreover, the reported stress level required for shear rupture is lower than the average rupture stress for cortex material in compression, where in radial and circumferential direction 0.25 and 0.18 MPa are reported. Generally an increase of the loading rate leads to an increase of rupture shear stress.

Fig. 11 Nominal shear stress versus relative vertical displacement measured by Farshad et al. (1999) in a small punch test of slowly loaded cortex samples (loading rate 5 mm/min)
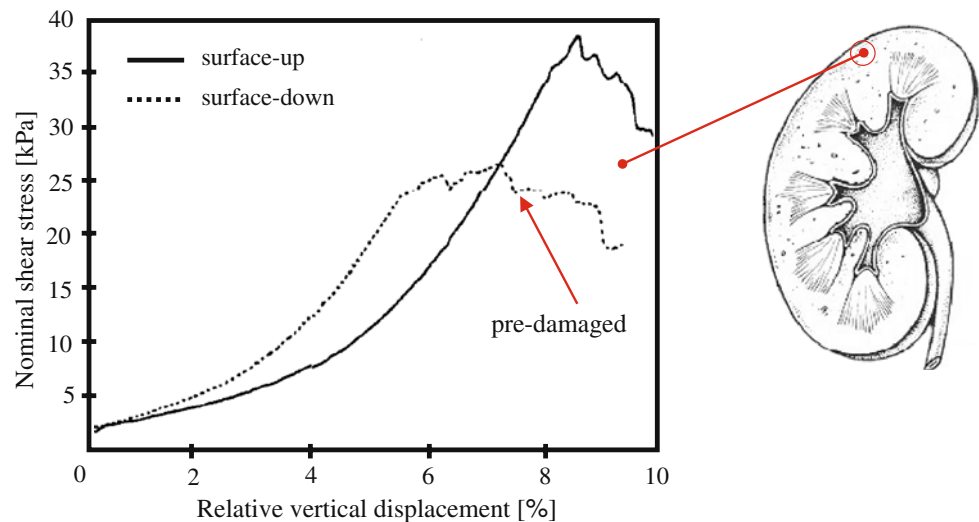
Nasseri et al. report in Nasseri et al. (2002) experiments on the renal cortex of fresh pig kidneys. Dynamic shear tests with small amplitude oscillatory motion (cycles) and shear rates between 0.01 and 2.5 s^{-1} were performed. The data were adapted to a model combining non-linear viscosity with two-parametric Odgen elasticity which was originally developed for brain tissue. We do not apply this model, because the viscous effects in the range of several seconds are not relevant for our application, but we refer to the measured data. Of particular interest for us is the observed rupture stress in shear ranging from 100 Pa up to 1,000 Pa. Again, an increase of rupture stress with the increase of shear rate was observed. However, all values are significantly lower than the values reported in Farshad et al. (1999).

Taking all the reported measurements into consideration, significant variations are observed. Note that there may also be a certain scale dependence, e.g., the rupture stress of renal tubulus (capillaries with 25–50 μm in diameter) was determined in Welling and Grantham (1972) to be 1.8–2 MPa. The difference of in vitro and in vivo data was pointed out in Gefen and Margulies (2004) and Maass and Kuehnapfel (1999). Moreover, clinical investigations observed renal damage in ESWL when the peak negative pressure exceeds 1.5–3.5 MPa (Coleman et al. 1995; McAteer et al. 2002). Concluding from these and further sources, we assume the threshold for damaging stresses in the kidney to be in the range of 20–2,000 Pa, where the cortex is less sensitive than the medulla and the (liquid filled) ureter is unlikely to be damaged at all, cf. Sect. 6 for details.

5 Material model

An ESWL treatment of a living kidney often correlates with a fall in renal function and the onset of hypertension. The reason for that is the special way a kidney works—which is, of course, more than a pure mechanical response on straining or shearing. The functional lesions clearly indicate irreversible changes in the soft tissue.

Translated into mechanical terms this means that the reversible (elastic) response of the material is bounded; above a certain bearable stress some kind of impairment (damage) occurs which we model here as a non-reversible deformation. To this end let the deformation of a material point at position x and instance t be fully described by the deformation gradient $F \equiv F(x, t)$ and let F^e denote its elastic and F^i its inelastic component. Both are related by

$$F = F^e F^i. \tag{6}$$

For the response of the kidney tissue on deformation, a constitutive relation is required. Because an approach going from the microscopic cell to the macroscopic level is not yet realistic (cf. Verdier 2003), such a constitutive relation is empirical and will model the tissue as a kind of homogenized material. For the elastic response we employed a two-parametric general Ogden material with strain energy density W^O (Holzapfel 2000),

$$W^O = \sum_{p=1}^{2} \frac{\mu_p}{\alpha_p}(\lambda_1^{\alpha_p} + \lambda_2^{\alpha_p} + \lambda_3^{\alpha_p} - 3), \tag{7}$$

where $\lambda_1, \lambda_2, \lambda_3$ are the principal stretches. The Ogden model describes by definition an incompressible material behavior. It needs to be extended to the compressible range by addition of a volumetric component of the strain energy density, W^{vol}. In this way the elastic strain energy density reads

$$W^e = W^O + W^{vol} \quad \text{with} \quad W^{vol} = \kappa(\log(\det F^e))^2/2. \tag{8}$$

The weighting coefficients in Eq. (7) are chosen in the same way as proposed in Miller et al. (2000), where a
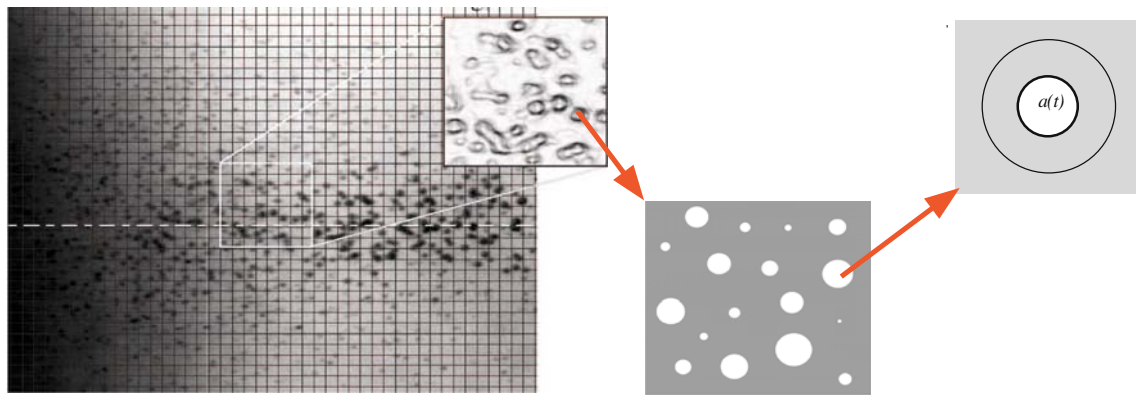
Fig. 12 Experimentally observed bubble cavitation in the focus of an ESWL lithotripter, cf. Bailey et al. (2003b), motivated the model of a soft tissue with pores of radius $a(t)$

two-parametric Ogden material law has been adapted to experiments with brain tissue, $\alpha_1 = 5$, $\alpha_2 = -5$ and $\mu_1 = \mu/15$, $\mu_2 = -\mu/3$. However, the shear modulus μ itself, which is given by the sum $(\alpha_1\mu_1 + \alpha_2\mu_2)/2$ is, of course, determined in correspondence to the elastic constants of the kidney tissues, $\mu = 3E\kappa/(9\kappa - E)$, cf. Sect. 3. The stresses follow from (8) by the derivative w.r.t. the deformation and transformation into the current configuration, $\boldsymbol{\sigma} = \partial W/\partial \boldsymbol{F}$ $(\det \boldsymbol{F})^{-1}\boldsymbol{F}^{-T}$.

The stresses are bounded by an upper limit, further deformation will alter the tissue irreversibly. As described in Sect. 2, inelastic deformation may happen by shearing (resulting in tearing) as well as by hydrostatic tension (resulting in pore growth). Consequently, we introduce two scalar variables accounting for irreversible damage *accumulated* by inelastic deformation, ε^i and ϑ^i. Their temporal developments (rates) are subjected to the constraints

$$\dot{\varepsilon}^i \geq 0 \quad \text{and} \quad \dot{\vartheta}^i \geq 0. \tag{9}$$

Inelastic shear induced deformation is commonly described by classical $J2$-plasticity which assumes plastic deformation to be volume preserving and described by the unimodular part of $\boldsymbol{F}^i$ only, cf. Simo and Hughes (1998). We follow this approach here and understand ε^i as a measure of *accumulated irreversible straining*. The *irreversible volumetric expansion*, which is induced by the cavitation of bubbles, is captured by ϑ^i and described by the volumetric part of $\boldsymbol{F}^i$. Consequently, the rate of inelastic deformation is constrained by the kinematic condition

$$\dot{\boldsymbol{F}}^i \boldsymbol{F}^{i-1} = \dot{\varepsilon}^i \boldsymbol{M} + \dot{\vartheta}^i \boldsymbol{N}, \tag{10}$$

where tensors $\boldsymbol{M}$ and $\boldsymbol{N}$ set the direction of the unimodular and volumetric inelastic deformation rates, respectively. Note that tensor $\boldsymbol{M}$ is normalized and unimodular, $|\boldsymbol{M}|^2 = 3/2$, $\text{tr}(\boldsymbol{M}) = 0$, but otherwise unknown, whereas tensor $\boldsymbol{N}$ is fixed, $\boldsymbol{N} = 1/3\boldsymbol{I}$. In that way tensor $\boldsymbol{N}$ corresponds to volumetric expansion and in compression the elastic defor-

mation will not be bounded. This approach corresponds to experimental observations from where we know that pressure does not damage the material but hydrostatic tension does (Sturtevant and Lokhandwalla 1998).

The special feature of this model, namely the damage by irreversible volumetric expansion, is motivated by the mechanisms of bubble cavitation. A detailed model of cavitation induced damage is outlined in Weinberg and Böhme (2008), here we will shortly summarize the basic ideas. From the mechanical point of view the (ESWL-treated) human kidney is a conglomerate of liquid-containing cells in which the hypersonic excitation activates the nucleation and oscillation of bubbles. Thus, we model the "soaked tissue" to be a soft solid in which initially very small bubbles are already embedded. Every bubble corresponds to a pore of radius $a(t)$ and is at every instance surrounded by a sphere of tissue material, see Fig. 12. The processes of bubble nucleation and coalescence are neglected. Moreover, all volumetric expansion of the composite is attributed to pore growth solely, the tissue itself is incompressible. From these simplifying assumptions the kinematics of pore expansion can be deduced for every single pore. Now, the modeling of the actual kidney tissue follows a *multi-scale* approach. The microscopic model describes bubble growth on the microscopic level, i.e., in a representative volume element located at given position $\boldsymbol{x}$. (Such a volume element is, e.g., the material at the integration points of finite elements.) The material in the volume element is modeled as assemblages of pores surrounded by tissue, and we presume the initial porosity as well as the initial pore size distribution to be known.

From the microstructural evolution in the volume element, a damage parameter is deduced. In the macroscopic model (e.g., the full finite element model of the kidney), internal variables "measure" the damaging effect of the applied load and deformation.

These internal variables can be related to the damage parameter of the microscopic process in a one-to-one manner.

(a)

(b)
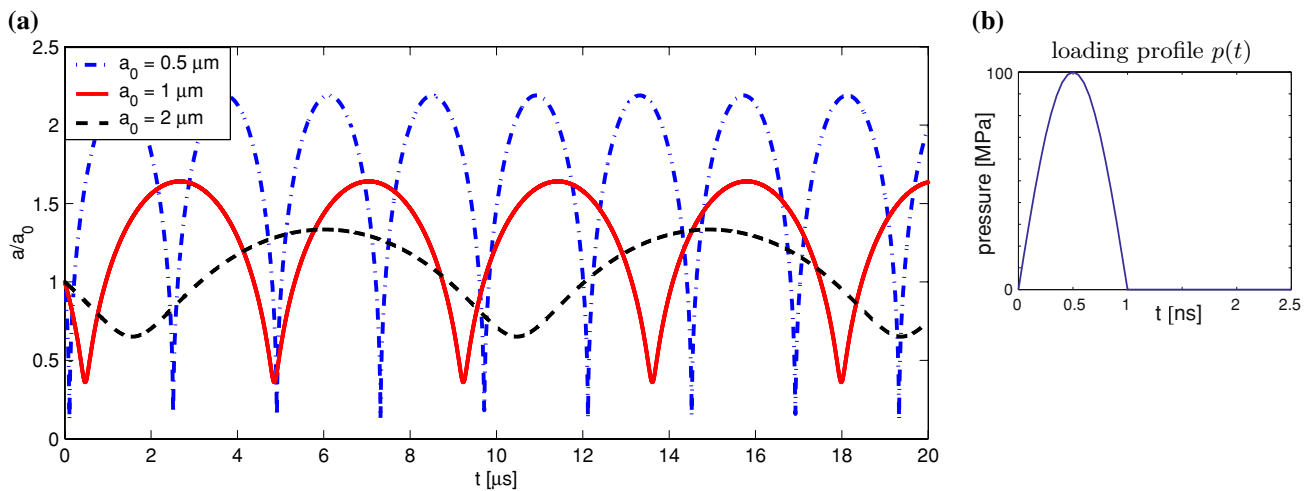
Fig. 13 Cavitation: **a** oscillation of bubbles with different initial radii in a soft elastic media enforced by an initial pressure, **b** pressure impulse of $p_{max} = 100$ MPa within $t_p = 1$ ns

Microscopic model: As a consequence of mechanical loading, the material of the volume element may expand and the pores grow in different ways. The power of the external forces P acting on the volume element is (assumed to be) completely compensated by the internal energy change accompanied with the deformation of the tissue and the expansion of the containing bubbles. Three forms of energy dominate here: (1) the elastic energy W^e of the deforming tissue material, (2) the kinetic energy K due to bubble expansion and (3) surface energy S stored in the interface between bubble and tissue. By means of the ansatz

$$P = \frac{\mathrm{d}}{\mathrm{d}t}(W^e + K + S) \tag{11}$$

we obtain an ordinary differential equation for every pore radius $a(t)$, see Weinberg and Böhme (2008) for more details. Solving this equation for different initial conditions yields a constitutive relation for bubble growth. In Fig. 13 a typical result is illustrated. Here we look at an ensemble of pores with initial radii of $a_0^{(1)} = 0.5\,\mu$m, $a_0^{(2)} = 1\,\mu$m and $a_0^{(3)} = 2\,\mu$m, distributed equally. Note that the computed bubble oscillations are very similar to the cavitation process observed in fluids and described by the Rayleigh–Plesset equation, cf. Fig. 3. Moreover, it is interesting to note, that the ratio of a_{max}/a_0 increases the smaller the initial pore is, whereas the periodic time of one oscillation decreases for a smaller initial pore radius.

However, in reality the cavitated bubbles will not remain spherical, but will collapse non-spherically, cf. Fig. 3b. Whereas nucleation of new bubbles could easily be incorporated in our model, the actual mechanisms of bubble collapse are a research topic of its own and not considered here.

Our interest here is only the *maximum* radius of the growing bubbles—which is likely to overstrain the surrounding vessels and capillaries. Therefore we deduce from the computed bubble sizes a macroscopic damage parameter. This parameter, $\vartheta(\boldsymbol{x}, t)$, indicates the local temporal evolution of irreversible material changes and is, by nature, a monotonic and continuous function of space and time. For the class of materials considered here, we suggest that the material is irreversibly strained and damage happens when a critical bubble radius a_{crit} is exceeded. (Here we set $a_{crit} = \max(a_0)$ but this value is to adapt to the specific material.) Then, because of the dissipative character of the damaging process, a bubble oscillation with constant amplitude (and with radii of $a > a_{crit}$) as illustrated in Fig. 13 is impossible. Instead, only the first maximal radius of every bubble can induce damage and subsequent oscillations are not of interest. Let us, therefore, define the damage parameter related to cavitation to be proportional to the maximal radii in the ensemble of bubbles

$$\vartheta(\boldsymbol{x}, t) \propto \sum_{\text{bubbles}} \log(\hat{a}(a, \boldsymbol{x}, t))$$

$$\text{with } \hat{a}(a, \boldsymbol{x}, t) = \max_{0 \leq \tau \leq t} a(\boldsymbol{x}, \tau). \tag{12}$$

With definition (12) bubble oscillation is only once considered to damage the material and only a next pressure impulse would raise the amount of damage again. This is what actually happens in an ESWL treatment where several (thousands) shocks are applied and damage is accumulated.

Macroscopic model: For the constitutive model in our FEAs we simplify the microscopic model and consider a volume element with a current *average* bubble radius $\bar{a}$, i.e., instead of a bubble distribution we watch the mean

values.[3] An initially undeformed volume of tissue V_0 has after expansion of bubbles a deformed volume V and the local volume fraction of bubbles can be determined as

$$f = N \frac{V_0}{V} \frac{4\pi \bar{a}^3}{3}, \tag{13}$$

where N is the referential bubble density, i.e., the number of bubbles per unit volume. The volumes V_0 and V are related through $V = J V_0$ where J is the local Jacobian of the deformation and J^e and J^i are the corresponding elastic and inelastic components.

$$J \equiv \det \boldsymbol{F} = \det(\boldsymbol{F}^e \boldsymbol{F}^i) = \det \boldsymbol{F}^e \det \boldsymbol{F}^i \equiv J^e J^i. \tag{14}$$

Using these relations, we can express the volume fraction of bubbles with the inelastic component of the Jacobian

$$J^i = \frac{V}{J^e V_0} = \frac{1 - f_0}{1 - f}. \tag{15}$$

Now express with Eq. (13) the initial and maximal volume fraction of bubbles and use the decomposition (14). Then, Eq. (15) may be recast in terms of the maximal averaged bubble radius, $\hat{\bar{a}}$, with the result

$$J^i = 1 - f_0 + \frac{V}{J^e V_0} f = 1 - N \frac{4\pi \bar{a}_0^3}{3} + N \frac{4\pi \hat{\bar{a}}^3}{3 J^e}. \tag{16}$$

It is known that $J^e \cong 1$ for the (almost) incompressible tissue material, and Eq. (16) simplifies to

$$J^i = 1 + \frac{4\pi}{3} N(\hat{\bar{a}}^3 - \bar{a}_0^3) \quad \text{and}$$

$$\hat{\bar{a}} = \left[\frac{3}{4\pi} \frac{1}{N} \left(J^i - 1 \right) + \bar{a}_0^3 \right]^{1/3}. \tag{17}$$

Relation $(17)_2$ allows $\hat{\bar{a}}$—which corresponds to the irreversible pore size in the tissue—to be computed from J^i. Consequently, we define in correspondence to (12) but now for the simplified approach

$$\vartheta^i = \log(J^i) = \log\left(1 + \frac{4\pi}{3} N(\hat{\bar{a}}^3 - \bar{a}_0^3)\right) \tag{18}$$

and obtain a clear physical meaning for the internal variable ϑ^i. It measures the accumulated inelastic volumetric deformation.

For implementation of the material model in our finite-element code we employ a time-incremental procedure similar to the one described in Weinberg et al. (2006) and Weinberg and Ortiz (2005). In every time step $t_{n+1} - t_n$ the internal state variables, ε_{n+1}^i and ϑ_{n+1}^i, are updated by

recourse to an incremental objective function $f_n = f_n(\boldsymbol{F}_{n+1}, \boldsymbol{F}_{n+1}^e, \varepsilon_{n+1}^i, \vartheta_{n+1}^i, \boldsymbol{M}, \boldsymbol{N})$. This function summarizes the elastic tissue energy (8), as well as the dissipated energy and the micro-kinetic energy of expanding bubbles. These energetic contributions [subject to the constraints (9 and 10)] compete among themselves, and the optimal internal process is that one which minimizes the function f_n.

The result of this energy minimization procedure is the current elastic and inelastic state of the material.
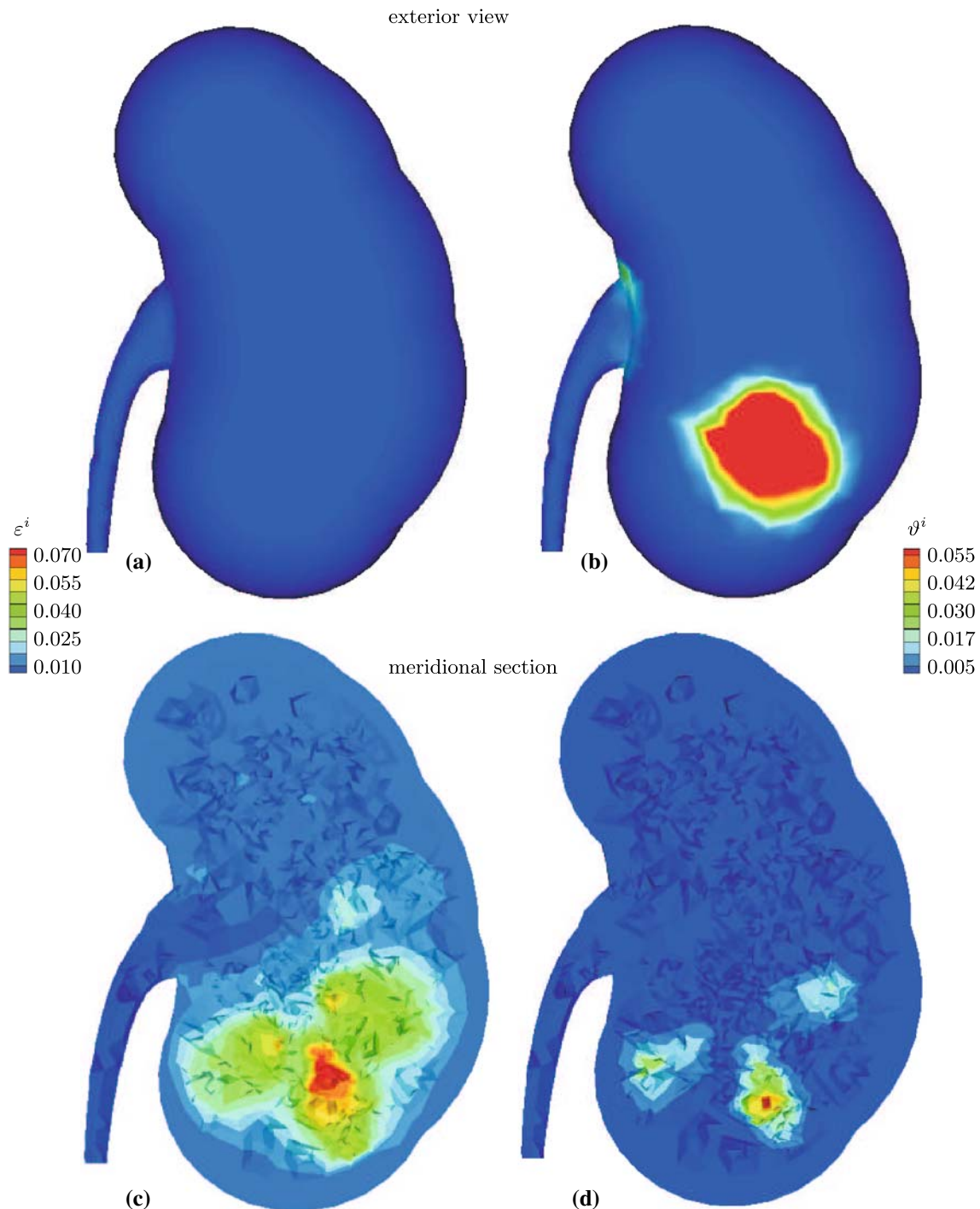
6 Numerical results

With all prerequisites in place we studied the response of the kidney tissue to ESWL shocks by means of several FEAs. The ESWL impulse is distributed along the boundary like a Gaussian distribution, as indicated in Fig. 6 for the two-dimensional model. In the three-dimensional model the impulse is applied on the anterior kidney surface and focused in the meridional section at $x = 0$, $y = 0$, $z = 10$ mm, see Fig. 7.

The spatial distribution on the anterior surface is again a Gaussian of radius 11 mm (centered at $x = 1$ mm, $y = 0$, $z = 17$ mm). Such a distribution correlates with measured data of Cleveland et al. (1998) and avoids artificial shear effects. For reasons of computational capacity not the full process of ESWL but the response of the material to *one* impulse was simulated.

The models are not supported. They are subjected to an impulse of form (1) with $p_{\max} = 50$ MPa applied as a nodal velocity via relation (4) and then released. For time integration we employ an explicit Newmark scheme with adaptive time step size over a period of $100\,\mu s$.

As described above in the model, regions of functional (sensitive) kidney tissue and non-functional tissue were distinguished. The sensitive structures, i.e., the cortex, the renal pyramids and the surrounding medulla tissue are modeled with the presented material model, the renal pelvis is presumed to behave elastically. The surrounding body tissue is modeled as an acoustic material with $\kappa = 2$ GPa. Recapitulating the reported experimental data, the limiting rupture stress values σ_0 were adapted to the different kidney regions in a similar manner as outlined for the elastic properties in Sect. 3. We choose here $\sigma_0 = 2$ kPa in the cortex, $\sigma_0 = 800$ Pa in the medulla tissue and $\sigma_0 = 25$ Pa within the renal pyramids and $a_0 = 1\,\mu m$, $f_0 = 0.001$ for all parts.

The results of 3d-FEAs are summarized in Fig. 14. We observe a good qualitative agreement of localized damaged regions with medical and experimental results. Shock waves induce lesions like kidney enlargement and bruising in the pre-focal area, see Coleman et al. (1995) and the photographs in Fig. 4. The location of injuries correlates to the area of peak negative pressure and greatest cavitation. This effect is well captured by our kidney model. Shear induced damage

---

[3] Please note that this simplification is only performed to reduce the computational effort. In principle the full microscopic model can be computed at the integration point level. The initial conditions (bubble radii and size distribution) can change from point to point in the material and so does its temporal evolution. The restriction to the mean radius implies that it grows monotonically to maximal radius $\hat{\bar{a}}$ within one impulse.

exterior view

meridional section

Fig. 14 Irreversible straining ε^i (**a, c**) and irreversible volumetric expansion ϑ^i (**b, d**) computed in the three-dimensional model of the kidney. The upper pictures (**a, b**) show the outside, the lower pictures (**c, d**) show the meridional section of the kidney

is observed in our model only within the kidney and hardly in the renal cortex, see Fig. 14.

To our knowledge there is no way to determine if the damage on the surface of the actual kidney is due to shear or volume expansion. But if the pressure is distributed like a Gaussian (what is measured, e.g., in Cleveland et al. 1998),

shearing should be of minor influence. However, it would play a role if the kidney surface is hit with a beam-like pressure impulse. In this case, the effect can be seen in computational simulations as well.

Furthermore, medical studies do not provide enough information to meter the degree of tissue damage. Typically such

studies correlate, e.g., the size of the kidney, the age of the patient or other parameters to the observed fall in renal function after an ESWL treatment. The exact location of the impulse hitting the kidney surface and further mechanical details of the treatment are usually not reported. Therefore it is hardly possible to *quantify* the tissue damage from the mechanical point of view.

Summarizing we can state that the highest damage occurs at the focus of the ESWL impulse. This is the position where typically the stone is located. In general, the presence of the stone, which is neglected here, will alter the pressure field of the surrounding tissue through reflection of the incident shock wave. Such reflection may even enhance tissue damage. On the other hand, experimental studies reported in Cleveland et al. (1998) did not find a significant influence of (the presence or absence of) a stone on the observed injuries caused by an ESWL treatment.

Because a quantitative assessment of the results is difficult to give we need to emphasize that the values computed for ϑ^i, ε^i and displayed in Fig. 14 actually should be scaled with (yet unknown) reference values of 'completely damaged tissue'. Moreover, after all we know the applied elastic material parameter can considered to be an upper bound of the materials elasticity in a rapid loading regime. This may, in part, overestimate the stresses (and the resulting damage) in our model. On the other hand, in that way a significant effect of one shock is visible. In practise, there are several hundred shocks applied and the damage within the kidney accumulates.

In an attempt to see the influence of the lithotripter device, we varied the (temporal) profile of ESWL impulse, $p(t)$. The original ESWL impulse as displayed in Fig. 2 is named *Church* impulse and is described by Eq. (1) with specified values of $\tau_1 = 1.1\,\mu s$ and $\tau_2 = 1.96\,\mu s$. Bailey (2002) and Matula et al. (2002) concluded from experimental

observations of an HM3 lithotripter that the actual impulse arriving at the focal point (in water) is somewhat stretched and better described by $\tau_1 = 1.96\,\mu s$ and $\tau_2 = 3.57\,\mu s$. Comparing the energy per area transported with a ESWL impulse (Wess 2004),

$$\frac{W}{A} = \frac{1}{\rho c_L} \int_{t_{\text{total}}} p(t)\mathrm{d}t \tag{19}$$

shows that the energy of a Bailey impulse is about 80% higher than the energy of the Church impulse. A possible consequence may be a more pronounced damage in the kidney tissue. For reason of comparison, we also apply to our model an *energy equivalent Church* impulse, i.e., an impulse with same energy transport as the Bailey impulse and $\tau_1 = 1.1\,\mu s$, $\tau_2 = 1.96\,\mu s$. The amplitude is then 90.9 MPa, see Fig. 15a.

The three different ESWL impulses were applied to a fine two-dimensional mesh with material data as above and viscosity parameter $\alpha = 0.06$. The cavitation induced irreversible volumetric expansion $\vartheta^{(i)}$ (damage) is displayed in Fig. 15b. It is induced here by the Bailey impulse, but its distribution is representative for all three ESWL impulses. For comparison the damage is quantified for two different initial bubbles sizes, Fig. 15c, the displayed values are scaled with the computed maximum, therefor. Note that the influence of the bubble radius in our model enters the result by the definition of a critical bubble radius for initiating damage, cf. Eq. (16).

The highest damage is observed for the energy equivalent Church impulse, whereas the differences of Church and Bailey impulse with same amplitude are small. This effect is very likely due to the greater tensile stress caused by the tail of the higher impulse. The initial compressive front does not directly cause damage but a higher tension would cause more cavitation, i.e., bubbles expand to a larger size.

(a) ESWL impulses   (b) location of damage   (c) relative damage
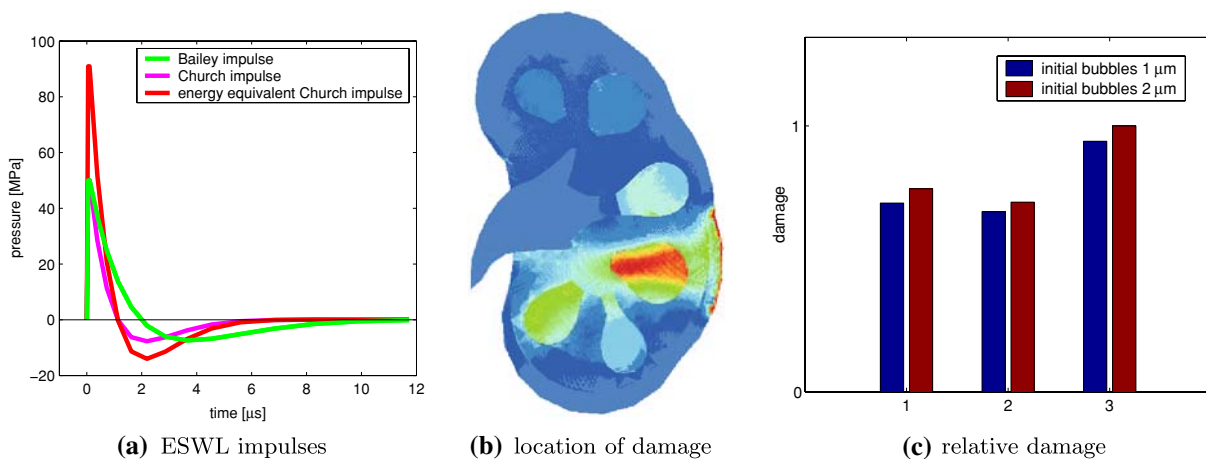
Fig. 15 Variation of the ESWL profile: **a** different shapes of ESWL impulse, **b** damage induced by a Bailey impulse in the 2d model and **c** comparison of the damaging effect of different wave profiles for two initial bubble sizes (1: Bailey impulse, 2: amplitude equivalent Church impulse, 3: energy equivalent Church impulse)
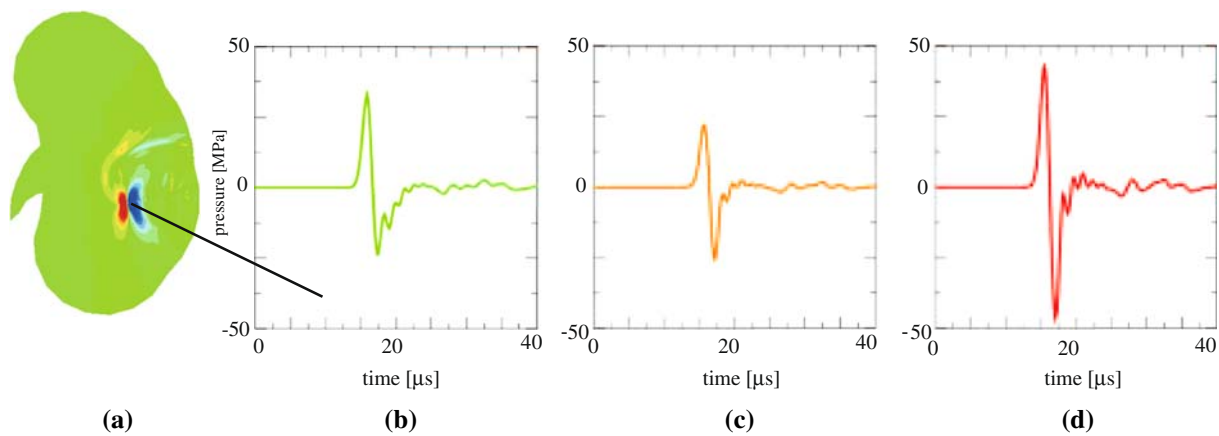
Fig. 16 Pressure state resulting from different ESWL impulses: **a** location of the measured impulse (*red*: compression, *blue*: tension), **b** Bailey impulse of 50 MPa amplitude, **c** amplitude equivalent Church impulse, **d** energy equivalent Church impulse

This implication is known from studies on bubble dynamics, which have shown that the amplitude of the tensile portion of the shock impulse is the major contributor to bubble growth, cf. Iloreta et al. (2007).

The exact details of the lithotripter waveform seems not to be as important for inducing volumetric expansion as the maximum value of pressure (and thus tension) of the ESWL impulse. To underline this result the actual magnitude of pressure arriving at the location of maximal damage is displayed in Fig. 16. It appeared that the decay of pressure amplitude in part correlates with the experimental data of Filipczynski et al. (1994). After about 40 mm of transmission the pressure maxima are 70% of the initial amplitude for the Bailey impulse and 50% for the amplitude equivalent Church impulse.

Moreover, a significantly enlarged tension tail is observed for both Church impulses. However, the energy of the impulse does not determine the damage but rather the magnitude of the tensile or compressive stresses. This will be the reason for the observation that an amplitude equivalent Church impulse induces almost the same volumetric damage as the longer Bailey impulse.

7 Conclusions

Summarizing we state that the presented numerical analysis of ESWL is a powerful tool for studying the effect of shock waves on soft tissue. The underlying material model describes the macroscopic constitutive behavior with a microscopic approach. With a detailed finite-element model of the kidney that maps the various structures individually and accounts for inelastic strain, cavitation and volume expansion we are able to predict the onset of damage in the kidney tissue. The damaged regions located by our model are in the focal and pre-focal area of the shock wave. These results compare well with medical and experimental findings. In particular, we are able to analyze the influence of form and energy of the ESWL impulse on the tissue. Our findings suggest that not the initial compressive pressure front of the shock wave induces tissue damage but rather the greater tensile stress caused by the tail of the impulse. Therefore, comparing two ESWL impulses with same energy transport the one with larger tensile amplitude is more destructive. Moreover, a bubble distribution with initially large bubbles magnifies the damaging effect of cavitation.

A significant refinement of the finite element models together with a variation of the initial conditions of straining and bubble cavitation will further improve the quality of the computational results. However, a simulation of a full ESWL process with several hundred shocks is limited by computational capacity. Nonetheless, our novel computational approach provides an efficient strategy to asses side effects of shock-wave lithotripsy treatments.

References

Bailey M (2002) Presentation at the meeting of the consortium for shock waves in medicine (unpublished), Indianapolis, IA

Bailey MR, Cleveland RO, Colonius T, Crum LA, Evan AP, Lingeman J, McAteer JA, Sapozhnikov OA, Williams JC (2003a) Cavitation in shock wave lithotripsy: the critical role of bubble activity in stone breakage and kidney trauma. In: Proceedings of IEEE Ultrasonics Symposium, pp 724–727

Bailey M, Crum L, Sapozhnikov O, Evan A, McAteer J, Cleveland R, Colonius T (2003b) Cavitation in shock wave lithotripsy. In: Proceedings of the 5th International Symposium on Cavitation, Osaka, Japan

Blomgren PM, Connors BA, Lingeman JE, Willis LR, Evan AP (1997) Quantitation of shock wave lithotripsy-induced lesion in small and large pig kidneys. Anat Rec 249(3):341–348

Brennen CE (1995) Cavitation and bubble dynamics (Oxford Engineering Science Series). Oxford University Press, New York

Brown SA, Munver R, Delvecchio FC, Kuo RL, Zhong P, Preminger GM (2000) Microdialysis assessment of shock wave lithotripsy-induced renal injury. Urology 56(3):364–368

Chaussy C, Schmiedt E, Jocham D, Brendel W, Forssmann B, Walther V (2002) First clinical experience with extracorporeally induced destruction of kidney stones by shock waves (reprinted from J Urol 127:417–420, 1981). J Urol 167(5):1957–1960

Cleveland RO, Lifshitz DA, Connors BA, Evan AP, Willis LR, Crum LA (1998) In vivo pressure measurements of lithotripsy shock waves in pigs. Ultrasound Med Biol 24(2):293–306

Coleman A, Saunders J (1993) A review of the physical-properties and biological effects of the high amplitude acoustic fields used in extracorporeal lithotripsy. Ultrasonics 31:75–89

Coleman AJ, Kodama T, Choi MJ, Adams T, Saunders JE (1995) The cavitation threshold of human tissue exposed to 0.2-mhz pulsed ultrasound—preliminary measurements based on a study of clinical lithotripsy. Ultrasound Med Biol 21(3):405–417

Connors BA, Evan AP, Willis LR, Blomgren PM, Lingeman JE, Fineberg NS (2000) The effect of discharge voltage on renal injury and impairment caused by lithotripsy in the pig. J Am Soc Nephrol 11:310–318

Deng YL, Luo DZ, Chen HG (1993) Effects of high-energy shock-waves on testes of wistar rats. J Endourol 7(5):383–386

Evan AP, Willis LR, Lingeman JE, McAteer JA (1998) Renal trauma and the risk of long-term complications in shock wave lithotripsy. Nephron 78(1):1–8

Farshad M, Barbezat M, Flueler P, Schmidlin F, Graber P, Niederer P (1999) Material characterization of the pig kidney in relation with the biomechanical analysis of renal trauma. J Biomech 32(4):417–425

Filipczynski L, Etienne J, Kujawska T (1994) Shock-wave pulse pressure after penetration of kidney tissue. IEEE Trans Ultrason Ferroelectr Freq Control 41(1):130–133

Gefen A, Margulies SS (2004) Are in vivo and in situ brain tissues mechanically similar?. J Biomech 37:1339–1352

Holzapfel G (2000) Nonlinear solid mechanics. Wiley, New York

Howle L, Schaefer DG, Shearer M, Zhong P (1998) Lithotripsy: the treatment of kidney stones with shock waves. SIAM 40:356–371

Iloreta IJ, Zhou Y, Sankin GN, Zhong P, Szeri AJ (2007) Assessment of shock wave lithotripters via cavitation potential. Phys Fluids 19(8):086103

Maass H, Kuehnapfel U (1999) Noninvasive measurement of elastic properties of living tissue. Institut für Angewandte Informatik, Forschungszentrum Karlsruhe

Matula T, Hilmo P, Storey B, Szeri A (2002) Radial response of individual bubbles subjected to shock wave lithotripsy pulses in vitro. Phys Fluids 14(3):913–921

McAteer J, Williams J, Willis L, Evans AE (2002) Personal communication with the autor (k.w.) at the SWL group meeting, Indianapolis, IA

Melvin JW, Stalnaker RL, Roberts VL (1973) Impact injury mechanisms in abdominal organs. SAE Trans (cited in Miller 2000) 700968:115–126

Miller K (2000) Constitutive modelling of abdominal organs. J Biomech 33:367–376

Miller K, Chinzei K, Orssengo G, Bednarz P (2000) Mechanical properties of brain tissue in-vivo: experiment and computer simulation. J Biomech 33:1369–1376

Nasseri S, Bilston LE, Phan-Thien N (2002) Viscoelastic properties of pig kidney in shear, experimental results and modelling. Rheol Acta 41:180–192

Plagemann M (2006) Numerische Untersuchungen zur Belastung der menschlichen Niere während einer Lithotripsie-Behandlung. Studienarbeit, Institut für Mechanik, TU Berlin

Schmidlin FR, Schmid P, Kutyka T, Iselin C, Graber P (1996) Force transmission and stress distribution in a computer simulated model of a kidney: An analysis of the injury mechanisms in renal trauma. J Trauma 40:791–796

Simo JC, Hughes TJR (1998) Computational inelasticity. Springer, Berlin

Sturtevant B, Lokhandwalla M (1998) Biomechanical effects of ESWL shock waves. J Acoust Soc Am 103:3037–3053

Tanguay M, Colonius T (2003) Progress in modeling and simulation of shock wave lithotripsy (SWL). In: Proceedings of the 5th International Symposium on Cavitation, Osaka, Japan, published electronically at http://iridium.me.es.osaka-u.ac.jp/cav2003/index1.html:paperOS-2-1-010

Thiel M, Nieswand M, Dorffel M (2000) The use of shock waves in medicine—a tool of the modern or: an overview of basic physical principles, history and research. Minim Invasive Ther Allied Technol 9(3–4):247–253

Verdier C (2003) Rheological properties of living materials. From cells to tissues. J Theor Med 5:67–91

Weinberg K, Böhme T (2008) Mesoscopic modeling for continua with pores: biological soft tissue. Non-equilibrium Thermodyn 33(1):1–25

Weinberg K, Ortiz M (2005) Shock wave induced damage in kidney tissue. Comput Mater Sci 32:588–593

Weinberg K, Mota A, Ortiz M (2006) A variational constitutive model for porous metal plasticity. Comput Mech 37(2):142–152

Welling LW, Grantham JJ (1972) Physical properties of isolated perfused renal tubules and tubular basement membranes. J Clin Invest 51:1063–1075

Wess O (2004) Physikalische Grundlagen der Stoßwellentherapie. J Mineralstoffwechsel 4:7–18

Willis LR, Evan AP, Connors BA, Blomgren P, Fineberg NS, Lingeman JE (1999) Relationship between kidney size, renal injury, and renal impairment induced by SWL. J Am Soc Nephrol 10:1753–1762

Wilson WT, Morris JS, Husmann DA, Preminger GM (1992) Extracorporeal shock-wave lithotripsy—comparison between stone and no-stone animal-models of SWL. J Endourol 6(1):33–36

Zhong P, Zhou Y, Zhu S (2001) Dynamics of bubble oscillation in constrained media and mechanisms of vessel rupture in SWL. Ultrasound Med Biol 27:119–134